Cosmic Voids in GAN-Generated Maps of Large-Scale Structure

Olivia Curtis[a,*], Tereasa G. Brainerd[a], Anthony Hernandez[b]

[a]*Department of Astronomy & Institute for Astrophysical Research, Boston University, Boston, MA 02215, USA*
[b]*Department of Computer Science and Engineering, University of South Florida, Tampa, FL 33620, USA*

Abstract

A Generative Adversarial Network (GAN) was used to investigate the statistics and properties of voids in a ΛCDM universe. The total number of voids and the distribution of void sizes is similar in both sets of images and, within the formal error bars, the mean void properties are consistent with each other. However, the generated images yield somewhat fewer small voids than do the simulated images. In addition, the generated images yield far fewer voids with central density contrast ~ -1. Because the generated images yield fewer of the emptiest voids, the distribution of the mean interior density contrast is systematically higher for the generated voids than it is for the simulated voids. The mean radial underdensity profiles of the largest voids are similar in both sets of images, but systematic differences are apparent. On small scales ($r < 0.5r_v$), the underdensity profiles of the voids in the generated images exceed those of the voids in the simulated images. On large scales ($r > 0.5r_v$), the underdensity profiles of the voids in the simulated images exceed those of the voids in the generated images. The discrepancies between the void properties in the two sets of images are attributable to the GAN struggling to capture absolute patterns in the data. In particular, the GAN produces too few pixels with density contrasts ~ -1 and too many pixels with density contrasts in the range ~ -0.88 to ~ -0.63.

Keywords: methods: numerical – methods: statistical – dark matter – large-scale structure of universe

1. Introduction

Galaxies are distributed within an interconnected, large-scale network of walls and filaments that stretch for hundreds of megaparsecs. Between these structures lie vast, underdense regions of space known as voids. Voids can reach up to $100h^{-1}$Mpc in diameter (see, e.g., Giovanelli and Haynes 1991 and references therein), and they have the potential to serve as excellent laboratories for testing the popular Λ Cold Dark Matter (ΛCDM) model of structure formation. Due to their underdense nature, voids are dominated by dark energy and they are only weakly influenced by the non-linear effects of gravity (see, e.g., Goldberg and Vogeley 2004). Because of this, the shapes and distributions of voids provide tests of modified theories of gravity, as well as constraints on the dark energy equation of state, inflationary models, the sum of the neutrino masses, and the expansion rate and geometry of the universe (see, e.g., Li et al. 2012, Sutter et al. 2012, Clampitt et al. 2013, Cai et al. 2015, Mao et al. 2017, Falck et al. 2018, Sahlén 2019). Furthermore, the physical properties of void galaxies provide critical insight into the history of galaxy formation and evolution (see, e.g., Hoyle et al. 2005, Kreckel et al. 2012, Douglass and Vogeley 2017, Tavasoli 2021) .

The total number of voids in existing void catalogs ranges from $\sim 10^2$ (e.g., Hoyle and Vogeley 2004, Sánchez et al. 2017) to $\sim 10^3$ to $\sim 6 \times 10^3$ (e.g., Mao et al. 2017, Aubert et al. 2020, Hamaus et al. 2017) Near-future surveys, such as those that will be carried out by the Vera C. Rubin Observatory (The LSST Dark Energy Science Collaboration et al. 2018), the Nancy Grace Roman telescope (Spergel et al. 2015), the Euclid satellite (Laureijs et al. 2011), the SPHEREx mission (Doré et al. 2018), the DESI experiment (DESI Collaboration et al. 2016), and the Prime Focus Spectrograph (Tamura et al. 2016) on the Subaru telescope, are expected to each yield void catalogs containing at least $\sim 10^5$ voids. This dramatic increase in data should lead to significant improvements in our understanding of the properties of voids and void galaxies in the observed universe.

From the standpoint of large-scale structure theory, gigaparsec-scale simulations are required in order to determine whether ΛCDM is able to successfully reproduce the largest structures in the universe. While Gpc-scale N-body mock catalogs do exist (e.g., Kim et al. 2011, Falck et al. 2021), the largest voids are so rare that only a few dozen of these objects are found within a single Gpc-scale simulation. N-body simulations of this size are computationally expensive to run, making it challenging to use these types of mock catalogs to fully investigate the statistics of the largest voids in ΛCDM universes. In order to make progress on the theoretical properties of the largest

---

*Corresponding author
Email address:* `amcurtis@bu.edu` (Olivia Curtis)

voids, it would be helpful to be able to use a modeling technique that is capable of quickly producing independent, novel catalogs of large-scale structure. One technique that may prove advantageous for such applications is the use of Generative Adversarial Networks (GANs).

GANs have already begun to demonstrate their usefulness for astrophysical applications. For example, Rodríguez et al. (2018), Curtis and Brainerd (2020), Feder et al. (2020), and Kodi Ramanah et al. (2020) used GANs to produce novel images of the large-scale structure of the universe. In addition, Mustafa et al. (2019) used GANs to generate novel weak lensing convergence maps. Further, Schawinski et al. 2017, Zingales and Waldmann (2018), and Gan et al. 2021 trained GANs to map observational data to either super-resolved data or denoised data, allowing computationally expensive Bayesian analyses to be bypassed in some cases.

In order for GANs to develop into computationally inexpensive alternatives to enormous, Gpc-scale N-body simulations, their efficacy in reproducing large-scale structure statistics must first be tested on smaller, more typical N-body simulations. Generally, the first assessment of GAN performance is a visual examination of the model's outputs (i.e., 'by-eye' inspection of the outputs). This is then followed by comparisons of lower-order and higher-order statistics for a generated sample and the training set. In the context of studies that use GANs to reproduce large-scale structure, lower-order statistics would include matter power spectra and/or mass density histograms (see, e.g., Rodríguez et al. 2018, Feder et al. 2020). Higher-order statistics would include Minkowski functionals such as those used by Mustafa et al. (2019) to assess their weak lensing convergence maps.

In this paper we explore the use of void statistics as a method of assessing the ability of a GAN to produce large-scale structure density maps. We examine the statistics and properties of voids in a ΛCDM universe, and we compare results obtained from N-body simulations to results obtained from a suitably trained GAN. Throughout, we search for voids in 2D slices of the large-scale structure to be consistent with modern observational void surveys (see, e.g., Sánchez et al. 2017, Mao et al. 2017). The paper is organized as follows. In §2, we discuss our computational methods. These include the N-body simulations that were used to train the GAN and the details of the particular GAN that we adopted. We also discuss the network architecture and optimization of the network weights. In §3 we discuss the underdensity probability function, the specific algorithm we used to identify voids, and various void properties. A discussion of our results is presented in §4. Throughout, we adopt the following cosmological parameters: $h = 0.7$, $\Omega_\Lambda = 0.7$, $\Omega_{m0} = 0.3$, and $\sigma_8 = 0.9$.

2. Methods

2.1. N-body Simulations

Before a GAN can be used to generate density maps of ΛCDM universes, it first must be taught the properties that are expected for the large-scale structure. Teaching the GAN these expected properties is a process known as training. Training the GAN requires a set of independent N-body simulations, the results of which allow the GAN to learn the expected properties of the large-scale structure and then to extrapolate from its training in order to produce new images. Here, the training set consisted of ten ΛCDM simulations. Each simulation adopted a cubical box with periodic boundary conditions, a box length of $L = 512h^{-1}\mathrm{Mpc}$, and a total of 512^3 dark matter particles of mass $m_p = 8.3 \times 10^{10}h^{-1}M_\odot$. A unique set of initial conditions for each simulation was generated using N-GenIC[1] (Springel et al., 2005) and the well-tested Gadget-2[2] code (Springel, 2005) was used to evolve the simulations from redshift $z = 50$ to the present epoch. All simulations were run on the Shared Computing Cluster at the Massachusetts Green High-Performance Computing Center.

To create a training set for the GAN, 15,000 2D images were extracted from the N-body simulations using the method adopted by Rodríguez et al. (2018). First, each simulation was divided each into 1,000 slices along each of the three primary axes. Each slice was then pixellated using a nearest neighbor mass assignment scheme and 500 non-consecutive slices along each axis were selected. Lastly, each image was smoothed with a Gaussian filter with a width of 1 pixel.

Note: while slices that are nearby to one another in a given simulation may be spatially correlated (i.e., sequential slices are separated by distances of $\sim 0.5h^{-1}\mathrm{Mpc}$), this is not expected to influence the training of the GAN in any significant way. During each training epoch, the order of the 15,000 slices is randomized and batches of 16 sequential images from the randomized slices are then fed to the network prior to back propagation (see Table 1). Because of this, it is unlikely that any of the 16 images in a given batch will have any remaining spatial correlation.

Before being passed to the GAN for training, the density maps from the N-body simulations must be normalized. This is necessary because normalizing reduces the cost of transforming the latent space distribution into the space expected of the true data distribution. Following Rodríguez et al. (2018), the density maps from the N-body simulations were normalized using

$$s(x) = \frac{2x}{x + a} \quad . \tag{1}$$

Here, a is an integer that controls the median pixel value of the normalized map, and the properties of $s(x)$ resemble those of a logarithmic function.

Feder et al. (2020) investigated the effect of changing the value of the scaling parameter in Equation 1 (a in our notation, κ in Feder et al. 2020). From this, Feder et al. (2020) found that larger values of the scaling parameter better preserved the high-density features in their generated density maps. On the small scales associated with galaxies, this gave rise to an improved agreement between the matter power spectra obtained from the generated images and the matter power spectra obtained from the N-body images. However, on the large scales that are relevant to cosmic voids, Feder et al. (2020) found that changes in the scale parameter had little affect on power spectrum from the generated images. Therefore, for consistency with Rodríguez et al. (2018) we adopt $a = 4$ throughout this paper. Examples of normalized 2D mass density maps, obtained from the N-body simulations, are shown in the top panels of Figure 1.

2.2. Generative Adversarial Networks

A GAN is a game between two deep convolutional neural networks: a discriminator network (D) and a generator network (G). The discriminator, $D : (\vec{x}, \theta_D) \rightarrow [0; 1]$, attempts to label a sample, $\vec{x}$, as being either 'real' or 'fake.' Here, 'real' means $\vec{x}$ is drawn from the true data distribution (p_{data}) and 'fake' means $\vec{x}$ is a generated image drawn from the set of generated data (p_{gen}). The variable θ_D represents the hyper-parameters that characterize D. The generator network, $G : (\vec{z}, \theta_G) \rightarrow \vec{x}$, attempts to map a random variable, $\vec{z}$, to a sample $\vec{x}$ that appears to be drawn from p_{data}. The random variable is drawn from a latent prior space, $p_{prior}(\vec{z})$, which is generally taken to be Gaussian-distributed.

The discriminator network is trained to maximize the probability of correctly labelling samples that are drawn from the training set and samples that are drawn from the generator network. Meanwhile, the generator network is trained to minimize $\log_{10}(1 - D(G(\vec{z})))$; i.e., the probability of the generator network producing a sample that the discriminator network mislabels as 'real'. Formally, D and G play what is known as the two-player minimax game:

$$\min_{G} \max_{D} \; [L(G_{\theta_G}, D_{\theta_D})] \qquad (2)$$

with loss function

$$L(G_{\theta_G}, D_{\theta_D}) := \mathbb{E}_{\vec{x} \sim p_{data}(\vec{x})}[\log_e D_{\theta_D}(\vec{x})] + \\ \mathbb{E}_{\vec{z} \sim p_{prior}(\vec{z})}[\log_e(1 - D_{\theta_D}(G_{\theta_G}(\vec{z})))] \;, \quad (3)$$

where $\mathbb{E}$ is the expectation function. (Note: Equation 3 reduces to the Jensen-Shannon divergence between p_{data} and p_{gen}; see Goodfellow et al. 2020.)

2.2.1. Wasserstein GANs

For our work, we adopted a particular type of GAN known as a Wasserstein GAN. The motivation for this choice stems from the phenomenon of mode collapse. Mode collapse is said to have occurred in a generative network when the generator produces only one particular output, regardless of its input. For example, suppose a GAN is being trained to generate pictures of rooms that would typically be found in a house (see, e.g., Gulrajani et al. 2017). Mode collapse occurs when the GAN only generates one image of a kitchen as its sole output.

Wasserstein GANs mitigate the problem of mode collapse by adopting what is known as an 'Earth mover's distance' loss function (see, e.g., Arjovsky et al. 2017). When applied to GANs, the Earth mover's distance allows the generator to find a more stable way of transforming p_{gen} into p_{data}. In return, the discriminator network now scores the 'realness' and 'fakeness' of an image (i.e., it scores how well p_{gen} resembles p_{data}). For this reason, Arjovsky et al. (2017) refer to the discriminator network as a 'critic network', a terminology that we also adopt. WGANs address the problem of mode collapse by not rewarding the generator network for its ability to generate a single result that consistently deceives the discriminator network, but by instead scoring the 'realness' and 'fakeness' of an image.

Additional discussion of Wasserstein GANs and the Earth Mover's distance is given in Appendix A and references therein.

2.2.2. Adam Optimizer

In order to carry out back propagation, we use a standard Adaptive Moment Optimizer known as *Adam* (see Kingma and Ba 2015). *Adam* is a stochastic gradient descent algorithm that updates the network weights using running averages of the first and second moments of the gradients of the loss function. The *Adam* optimizer is a popular choice for performing stochastic gradient descent because it is computationally efficient and has low memory requirements.

For given a set of parameters, $w^{(t)}$, and a loss function, $L^{(t)}$, at training iteration, t, the weights at the $t+1$ training iteration are found by first calculating the biased first and second moments using Equations 4 and 5, respectively:

$$m_w^{t+1} \leftarrow \beta_1 m_w^t + (1 - \beta_1) \nabla_w L^t \qquad (4)$$

$$v_w^{t+1} \leftarrow \beta_2 v_w^t + (1 - \beta_2)(\nabla_w L^t)^2. \qquad (5)$$

Here, β_1, $\beta_2 \in [0,1)$ are the exponential decay rates for the moment estimates, $m_w^{(t)}$ are the biased first moment estimates of the weights at step t, $v_w^{(t)}$ are the biased second moment estimates, and ∇_w is the gradient operator with respect to the network parameters.

Typical values for β_1 and β_2 are 0.9 and 0.999, so if m_w^0 and v_w^0 are initialized to zero, a significant bias towards small values in future updates will occur. This bias can be eliminated (making the moments less sensitive to β_1 and β_2 at early timesteps) by normalizing the β's such that $\sum_{i=0}^t \beta^i = \frac{1 - \beta^t}{1 - \beta}$. This normalization can then be removed by dividing the first and second moments by $1 - \beta^{t+1}$ in
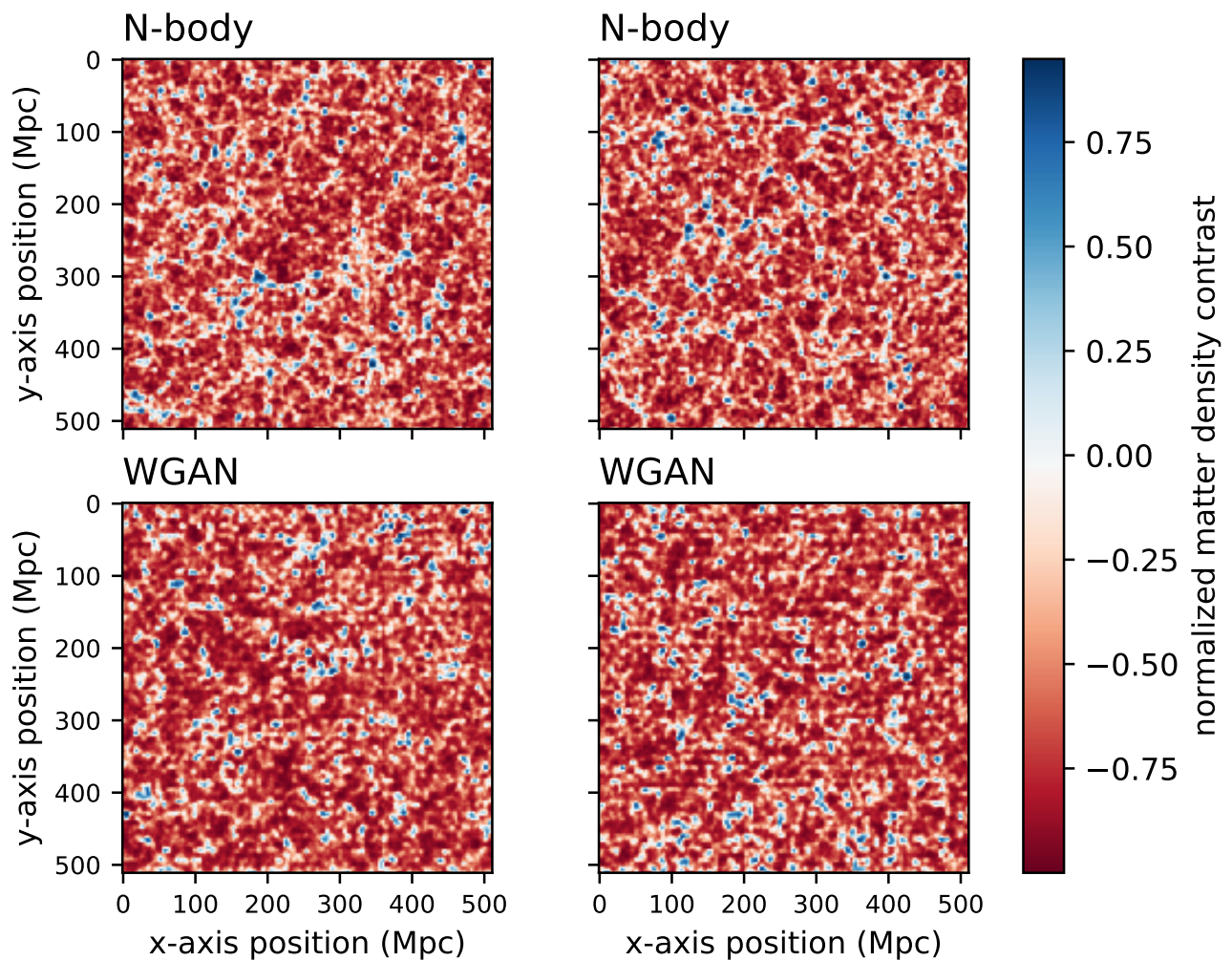
Figure 1: Examples of normalized matter density maps (i.e., 'images') at redshift $z = 0$. Each image has a sidelength of $512h^{-1}$ Mpc and a thickness of $0.512h^{-1}$Mpc. *Top:* Images obtained from N-body simulations. *Bottom:* Images obtained from a trained Wasserstein GAN (WGAN). Here the local matter density has been normalized using Equation 1 (see text).

Equations 6 and 7 below:

$$\hat{m}_w = \frac{m_w^{t+1}}{1 - \beta_1^{t+1}} \tag{6}$$

$$\hat{v}_w = \frac{v_w^{t+1}}{1 - \beta_2^{t+1}} . \tag{7}$$

Finally, the weights at step $t+1$ are calculated from the unbiased moments using

$$w^{t+1} \leftarrow w^t - \alpha \frac{\hat{m}_w}{\sqrt{\hat{v}_w} + \epsilon}, \tag{8}$$

where α is the algorithm's learning rate and ϵ is a small number that is used to prevent division by zero. Table 1 lists the values of the hyperparameters that we adopted for our work.

2.2.3. Network Architecture

Throughout, we use a standard WGAN architecture with deep convolutional layers. Details of the architecture are summarized in Table 2. The critic takes an image of size 256×256 pixels as its input. Four 2D convolutional layers then down-sample the image. The output of the critic is a score in the range $(-1, 1)$, which describes how 'real' (-1) or 'fake' $(+1)$ the critic thinks the image is. For the convolutional layers, a 4×4 pixel kernel with a stride of size $(2, 2)$ is used. In addition, the inputs of the network are batch normalized before each mini-batch update. The first four convolutional layers have a Leaky Rectified Linear Unit (Leaky-ReLU) activation function, and the last layer has a linear activation function. The first hidden layer down-samples the image into a tensor of shape $128 \times 128 \times 64$, where the last dimension is the number of channels. Each consecutive hidden layer then doubles the number of channels to 128, 256, and 512 respectively.

The generator takes a random 1D Gaussian vector of length 200 as its input. The first hidden layer is a linear layer that reshapes the latent space vector into a tensor of shape $16 \times 16 \times 512$ (i.e., 512 low resolution images of size 16×16 pixels). Four 2D convolutional transpose layers up-scale the image while reducing the number of channels. The first four layers use a ReLU activation function and have their inputs batch normalized before each mini-batch update. The output of the generator is an image of size 256×256 pixels where each pixel is cast into the range $(-1, 1)$ using a hyperbolic tangent function. To initialize the weights of the critic and generator, a Glorot weight initialization was used. This initializes each weight as a random number, pulled from a normal distribution that is centered on 0 and bounded by the inverse square root of the number of inputs to that node (see, e.g., Glorot and Bengio 2010).

The networks were implemented using Python's TensorFlow[3] package (e.g., Oliphant 2007; Abadi et al. 2016)

and were trained on two NVIDIA Tesla P100 graphics processing units with compute capability 6.0. The critic and generator networks had 2.89 million and 16.00 million trainable parameters, respectively. Training was carried out with Python version 3.7.7, TensorFlow version 1.15.0, CUDA version 10.0, and NVIDIA cuDNN version 7.6, and took approximately four hours for 20 training epochs. The implementation of the WGAN described in this paper is available on the first author's GitHub page.[4]

3. Results

The WGAN was trained for 20 epochs and the network parameters were saved after each training epoch. After 20 epochs, the outputs of each saved network were analyzed to determine which training epoch produced matter power spectra that were most similar to the training set. In the case of our WGAN, we found this to occur after four training epochs. This network was then used to generate a set of 15,000 density maps (i.e., 'images') which were used for the analyses we present below. Two of these generated images are shown in the bottom panels of Figure 1.

By eye, the images in Figure 1 that were obtained using the WGAN clearly resemble those that were obtained using N-body simulations. To assess differences in the two sets of images that may be present at a level that is too low to be detected by eye, we compute two statistics: [1] the distribution of the normalized matter density contrast in the individual image pixels and [2] the matter power spectrum.

The top panel of Figure 2 shows the normalized probability distribution for the matter density contrast in the individual pixels. All generated and simulated images were used to construct the probability distribution. The bottom panel of Figure 2 shows the ratio of the probabilities in the top panel. Error bars were computed using using 10,000 bootstrap resamplings of the data and are omitted when they are comparable to or smaller than the data points.

From Figure 2, we can see that, compared to the N-body results, the WGAN significantly under produces pixels that have the highest density contrast. These pixels are, however, relatively rare occurrences in the images (i.e., they have low probability) and they do not occur within voids. Potentially more problematic for void statistics are discrepancies between the frequencies at which pixels with the lowest density contrasts (i.e., the most underdense pixels) occur. These underdense pixels are the most common occurrences in the images (i.e., they have high probability), and differences in the distribution of density contrasts within these pixels should lead to slightly different statistics for both the central density contrast and the mean interior density contrast when we compare voids in the N-body images to voids in the GAN-generated images. Compared to the N-body results, the WGAN under

---

Table 1: Hyperparmeters used in the *Adam* optimizer, as well as other important network parameters (see Table 2)

Hyperparameter	Value	Description
Batch Size	16	Number of training samples fed into the network before back propagation
$\mathbf{z}$ dimension	200	Dimension of the random Gaussian vector
α_D	1e-6	Learning rate for the discriminator's (D) *Adam* optimizer
$\beta_{1,D}$	0.5	First exponential decay rate for D's *Adam* optimizer
$\beta_{2,D}$	0.999	Second exponential decay rate for D's *Adam* optimizer
α_G	5e-5	Learning rate for the generator's (G) *Adam* optimizer
$\beta_{1,G}$	0.5	First exponential decay rate for G's *Adam* optimizer
$\beta_{2,G}$	0.999	Second exponential decay rate for G's *Adam* optimizer
α	0.8	Momentum used in batch normalization
n_{disc}	5	Number of times D is updated for every G update
c	0.01	Weight clipping parameter used to uphold Lipschitz continuity in WGAN architectures
$\alpha_{LeakyReLU}$	0.2	Negative slope coefficient for LeakyReLU activation functions

Table 2: WGAN network architecture used in this paper

Layer	Operation	Output	Dimension
Critic			
$\mathbf{X}$			256 x 256 x 1
D_0	Conv2D	LeakyReLU-BatchNorm	128 x 128 x 64
D_1	Conv2D	LeakyReLU-BatchNorm	64 x 64 x 128
D_2	Conv2D	LeakyReLU-BatchNorm	32 x 32 x 256
D_3	Conv2D	LeakyReLU-BatchNorm	16 x 16 x 512
D_4	Linear	Linear	1
Generator			
$\mathbf{Z}$			200 x 1
G_0	Linear	ReLU-BatchNorm	16 x 16 x 512
G_1	Conv2D Transpose	ReLU-BatchNorm	32 x 32 x 256
G_2	Conv2D Transpose	ReLU-BatchNorm	64 x 64 x 128
G_3	Conv2D Transpose	ReLU-BatchNorm	128 x 128 x 64
G_4	Conv2D Transpose	Tanh	256 x 256 x 1

produces pixels with the lowest density contrast (i.e., the likely void centers) and over produces pixels with density contrasts in the range ~ -0.88 to ~ 0.63. This will lead to systematic differences in the distributions of the mean central densities and mean interior densities of the voids in the simulated and generated images.

Figure 3 shows the results for the matter power spectra of our simulated and generated datasets. The power spectra were calculated via

$$\langle \hat{\delta}(\vec{k})\hat{\delta}(\vec{k}') \rangle = (2\pi)^3 \delta_{\mathrm{D}}(\vec{k} - \vec{k}')P(\vec{k}) \qquad (9)$$

(see, e.g., Davis et al. 1985) and they encompass distance scales that are typical of void sizes (i.e., $10 - 100 h^{-1}\mathrm{Mpc}$). Here, $\delta_{\mathrm{D}}(\vec{k})$ is the Dirac delta function, $P(\vec{k})$ is the 1D matter power spectrum, and $\hat{\delta}(\vec{k})$ is the discrete Fourier transform of our density contrast field, defined as

$$\delta = \frac{n}{\overline{n}} - 1 \quad . \qquad (10)$$

Here n is the number of particles in a cell and $\overline{n}$ is the mean number of particles in a field. The discrete Fourier transform was computed with Python's NumPy[5] package (Walt et al., 2011). Points in the top panel of Figure 3 show the mean power spectra, computed using all simulated and generated images. Error bars were obtained from 10,000 bootstrap resamplings of the data. Points in the bottom panel of Figure 3 show the ratio of the mean power spectra from the simulated images to the mean power spectra from the generated images. From Figure 3, $P(k)$ from the generated images agrees with $P(k)$ from the simulated images on scales $< 20 h^{-1}\mathrm{Mpc}$. On larger scales, however, the generated images yield systematically lower values of $P(k)$ than do the simulated images.

3.1. Underdensity Probability Function

In the observed universe, the Void Probability Function (VPF) is commonly used to determine whether a randomly selected region in an image is devoid of galaxies (e.g., White 1979; Lachieze-Rey et al. 1992; Vogeley et al. 1994). The VPF depends on the galaxy N-point correlation function via

$$P_0(N, A) =$$
$$exp\left[\sum_{N=1}^{\infty} \frac{(-n)^N}{N!} \int_A w_N(\vec{x}_1, ..., \vec{x}_N) d^2 x_1 ... d^2 x_N \right] \qquad (11)$$

(e.g., White 1979), where n is the average number density of galaxies in the field, w_N are the N-point correlation functions, and $\vec{x}_i$ are the i-th galaxy positions in the area A.

Since our GAN outputs consist of images of a smoothed mass density distribution (i.e., not the locations of individual galaxies or individual particles) we do not compute the
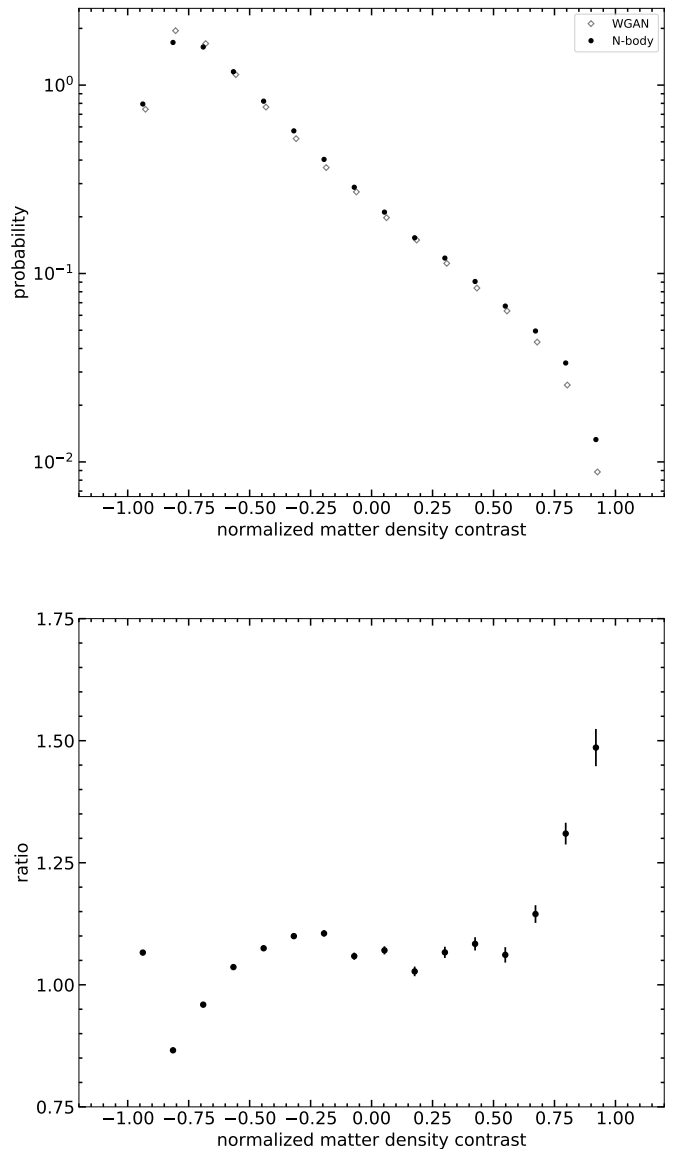

Figure 2: **Top:** Normalized probability distributions for the matter density contrast in the individual pixels of the images. Diamonds: results from 15,000 images generated with a WGAN. Circles: results from 15,000 simulated images. Error bars are omitted when they are comparable to or smaller than the sizes of the data points. **Bottom:** Ratio between the probability distributions shown in the top panel.
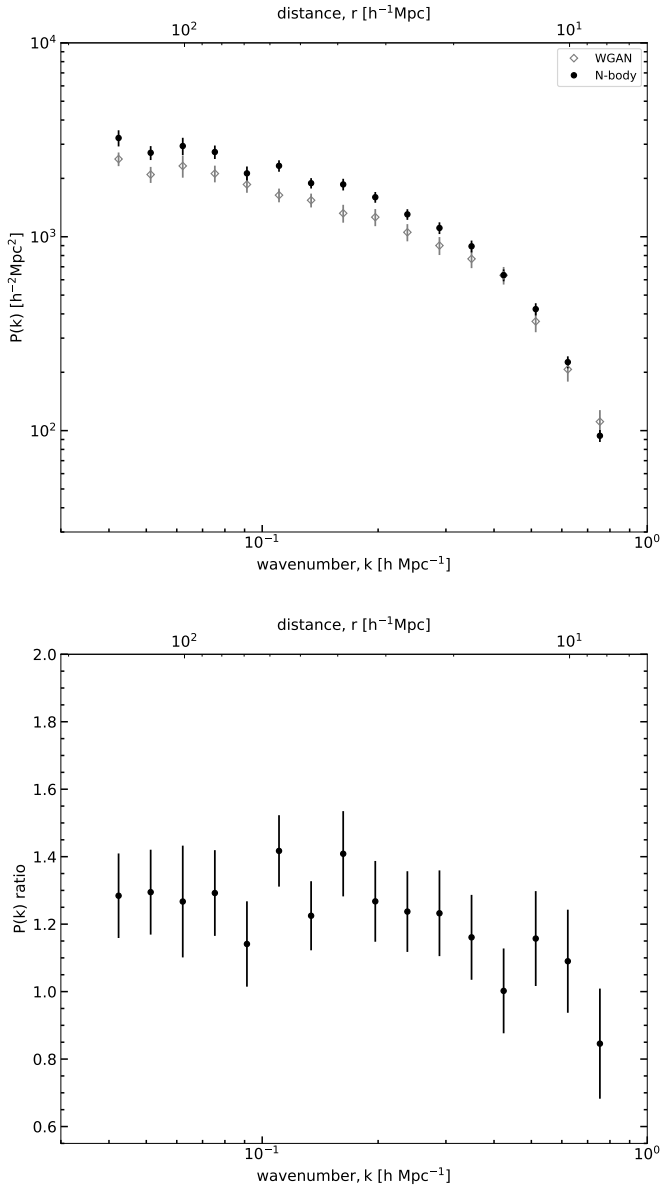

Figure 3: **Top: Mean matter power spectra, $P(k)$, computed from 15,000 simulated images (circles) and 15,000 images generated with a WGAN (diamonds). Error bars were computed using 10,000 bootstrap resamplings of the data. Bottom: Ratio of the mean matter power spectra shown in the top panel.**

VPF. Instead, we compute a similar statistic known as the Underdensity Probability Function (UPF; see, e.g., Vogeley et al. 1994 and Tinker et al. 2006). The UPF measures the probability that, within an area of radius r, a randomly selected region of space is less dense than some particular threshold density. An advantage to using the UPF over the VPF is that the VPF is sensitive to shot noise because it requires counting individual particles or galaxies within a given aperture.

To identify underdense regions in the density maps, we define a normalized density contrast $\Delta \equiv \frac{\delta\rho}{\rho}$ and we adopt a threshold for the mass density contrast of $\Delta < -0.6$. Here ρ is the local matter density and $\delta\rho$ is the difference between the local matter density and mean matter density of the image. That is, the UPF is defined as $U(r) = P(\Delta < \Delta_{\text{crit}}; r)$ where $\Delta_{\text{crit}} = -0.6$. The value of $\Delta_{\text{crit}} = -0.6$ was chosen to match the mean void underdensities reported in Hamaus et al. (2014) and Sánchez et al. (2017).

The UPF for the simulated and generated images was determined by computing the mean mass density contrast within randomly-placed circles of radius r. If the average density contrast within a circle of radius r is less than Δ_{crit}, then that particular region qualifies as being sufficiently underdense to be included in the calculation of the UPF. A total of $N_{\text{test}} = 10^4$ random circles of radius r were placed within each image and the total number of underdense regions, N_0, was then computed. The UPF was then defined as $U(r) = N_{(0;\ \Delta < \Delta_{\text{crit}})}/N_{\text{test}}$.

Figure 4 shows the mean UPF obtained from 15,000 simulated images and 15,000 generated images. The UPFs were calculated following the steps described above and error bars were calculated by bootstrap resampling of both sets of distributions. Note that, since smaller circles in an image are encompassed by larger circles in the same image, the data points in Figure 4 are not independent of one another. Hence, the point-to-point scatter is considerably smaller than the formal, bootstrapped error bars. Similar to the power spectra, there is good agreement between the simulated and WGAN images on small scales. On larger scales, there is a lower chance of finding underdense regions in the generated data than in the simulated data, with the difference increasing for regions $\geq 60h^{-1}$ Mpc.

3.2. Void Identification

To identify voids, we adopted a *voidfinder* algorithm that is similar to the algorithm used by El-Ad and Piran (1997) and Hoyle and Vogeley (2004) to identify voids in catalogs of galaxies. When applied to an observational dataset, the *voidfinder* algorithm identifies voids using the observed locations of galaxies. In our case there are no galaxies in the images. Instead, the images consist of pixels with known values of the mass density. Our version of the *voidfinder* algorithm, therefore, scans images of the large-scale structure as defined by the pixellated mass density.
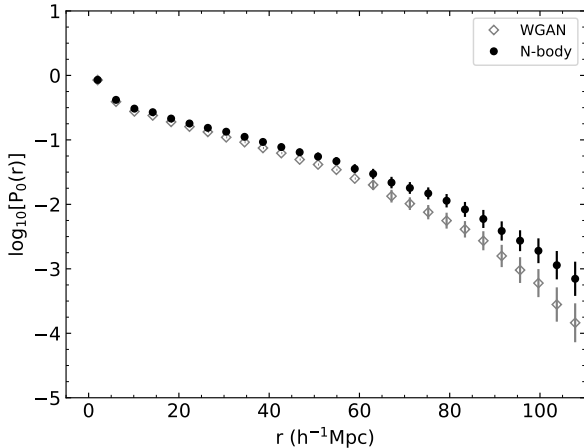
Figure 4: Mean underdensity probability function for images obtained from the simulated images (circles) and the WGAN-generated images (diamonds). Error bars were computed from 10,000 bootstrap resamplings of the data and are omitted when they are comparable to or smaller than the data points.

The algorithm yields a set of individual void centers and a list of which pixels in a given image belong to which voids.

Our *voidfinder* algorithm can be summarized in four steps: [1] each pixel is classified as being either a 'wall pixel' or a 'void pixel', [2] the distance between every void pixel and the nearest wall pixel is calculated, [3] void centers are defined to be the locations of the most isolated void pixels (i.e., the void pixels that are farthest from a wall pixel), and [4] as part of the process of identifying underdense regions that are interconnected, the areas of the larger voids are 'enhanced' to include overlapping regions of low mass density. The first step is performed by scanning over every pixel in the image using a circular aperture of radius $d = 3$ pixels that takes the periodic boundary into account. A value of $d = 3$ pixels (or $6h^{-1}$ Mpc) was chosen as a sensible size scale with which to judge a pixel's local environment.

If the pixel that the circular aperture is centered on contains at least $N = 9$ pixels with a normalized density contrast > -0.6, the pixel is classified as a 'wall pixel'. That is, if $\sim d^2$ of the pixels in the neighborhood around the central pixel are sufficiently dense compared to the mean, the central pixel is classified as a wall pixel. Any pixel that is not classified as a wall pixel is classified as a 'void pixel.' The second step is to iterate over each void pixel and determine its distance to the nearest wall pixel. This is done by finding the circle of maximum radius that can be centered around each void pixel such that the circle contains no wall pixels. Following the terminology of Hoyle and Vogeley (2004), we refer to these maximal circles as 'holes'.

Once all of the pixels have been classified as being either a void pixel or a wall pixel, the void centers are then identified. To do this, we begin by sorting all holes in a given image from largest to smallest in terms of their radii. We then define the center of the largest hole in the image to be the center of the first void. Having found this first void center, we then iterate over all holes. If the next hole in the sorted list overlaps with any previously-identified void by more than 10% of its own area, that hole is not considered to be an individual void and, at this point, is temporarily ignored. A value of 10% was chosen to insure only the largest hole in a local area is classified as a void, while still accounting for smaller voids that interconnect the larger voids. If the next hole in the sorted list does not overlap with any previously-identified void (or if the overlap is $\leq 10\%$ of its own area), the hole is classified as a distinct void, with the center of the hole being the void center. This process continues until all holes with radius > 3 pixels have been considered.

In order to account for the fact that underdense regions of space are interconnected, the final step in the process of identifying the voids is to consider the degree of overlap between holes and voids. The process is intended to examine the underdense regions near the edges of the holes and either assign those underdense regions to appropriate voids or reject them as being part of a void. If a hole overlaps a single void by $> 50\%$ of its own area (i.e., if the center of the hole is within the void's maximal hole), then we consider the hole to be part of the void. If a hole overlaps multiple voids by $> 50\%$ of its own area, we consider it to be part of the largest overlapping void. If a hole overlaps a void by $\leq 10\%$ of its own area, then the hole is identified as a distinct void, but the area of overlap is assigned to the larger void. If the overlap between a hole and a void is $> 10\%$ of the hole's area but $< 50\%$, the pixels in the hole are not assigned to any void. By this process, the total areas of the larger voids are enhanced relative to the areas of the maximal circles that are centered on the void centers.

Figure 5 shows the results of the *voidfinder* algorithm as applied to a single image. The different panels of Figure 5 show: a) the normalized density contrast, b) the locations of wall pixels (white) and void pixels (black), c) the distance to the nearest wall pixel at each location (i.e., the maximal radius for each pixel), d) the largest holes (i.e., the circles that define the void centers) overlaid on the density contrast, e) the largest holes overlaid on the wall/void pixel image, f) the locations of the largest holes overlaid on the distance to the nearest wall pixel, g) the final void areas overlaid on the wall/void pixel image, and h) same as g), but with the largest holes indicated. The 15,000 images from the N-body simulations yielded a total of 2.5 million voids and the 15,000 generated images yielded a total of 2.8 million voids. The mean number of voids contained within a single image from the N-body simulations (169 ± 10) is, however, consistent with the mean number of voids contained within a single generated image (184 ± 11).

3.3. Void Properties

Below we adopt the following terminology when discussing the void properties. The 'radius' of a void is simply the radius of the void's maximal circle (i.e., the largest circle, centered on the void center, with radius equal to the distance to the nearest wall pixel). The 'effective radius' of a void corresponds to the radius of a circle that, after the area of the void has been adjusted for any overlaps, is equal to the final area assigned to the void. Since some of the smaller voids lose area to neighboring large voids, their effective radii will be less than the radii of their maximal circles. Conversely, the larger voids with areas that have been enhanced by the addition of pixels from neighboring small voids (or significantly overlapping holes) will have effective radii that are larger than the radius of their maximal circle.

The top panels of Figure 6 show normalized probability distributions for a) the void radii and b) the effective void radii. Overall there is good agreement between the results for the simulated and generated images. Compared to the simulated images, however, the generated images produce fewer of the smallest voids. The median void radius in the generated images is identical to that of the simulated images ($10.0h^{-1}$ Mpc), but the median effective void radius in the generated images ($10.0h^{-1}$ Mpc) is somewhat larger than it is in the simulated images ($9.6h^{-1}$ Mpc). Figure 6c) shows the normalized probability distributions for the density contrast at the centers of the voids. Here, again, the distributions are similar and the median value of the central density contrast is nearly identical for the simulated and generated images (-0.83 in the simulated images vs. -0.81 in the generated images). However, compared to the simulated images, the generated images produce far fewer voids in which the central density contrast is ~ -1 (i.e., the most underdense void centers). Conversely, the generated images produce somewhat more voids with central density contrasts between ~ -0.9 and ~ -0.5 than do the simulated images. Figure 6d) shows the normalized probability distributions for the mean density contrast within the voids. While the median values of the distributions in Figure 6d) are similar (-0.79 for the simulated images vs. -0.76 for the generated images), there is a clear offset between the two distributions such that the mean density contrast of the generated voids is systematically higher than that of the simulated voids.

The results in Figure 6c) and 6d) are tied directly to the results in Figure 2. That is, compared to the simulated images, the generated images contain systematically fewer of the least dense pixels. Since voids are centered on the least dense pixels, this results in fewer voids in the generated images with central density contrasts ~ -1. It also results in fewer voids in the generated images having mean interior densities $\lesssim -0.8$. The combination of the generated images having both fewer of the least dense pixels and more of the pixels with density contrasts in the range ~ -0.88 to ~ -0.63 gives rise to more voids with

mean interior density contrasts $\gtrsim -0.7$ in the generated images

When averaged over all voids, the mean properties of the voids in the simulated and generated images are consistent within the formal error bars. In the simulated images, the mean radius and the mean effective radius are $9.9 \pm 0.2h^{-1}$ Mpc and $10.3 \pm 0.2h^{-1}$ Mpc, respectively. In the generated images, the mean radius and mean effective radius are $10.1 \pm 0.2h^{-1}$ Mpc and $10.5 \pm 0.2h^{-1}$ Mpc, respectively. In the simulated images, the mean central density contrast and the mean interior density contrast are -0.81 ± 0.01 and -0.79 ± 0.01, respectively. In the generated images, the mean central density contrast and the mean interior density contrast are -0.78 ± 0.02 and -0.76 ± 0.02, respectively. We note that, while the dispersions in the mean radius and the mean effective radius are identical for the voids in the simulated and generated images, the dispersions in the mean central density contrast and the mean interior density contrast are twice as large for the voids in the generated images as they are for the voids in the simulated images.

3.4. Properties of the Largest Voids

For the remainder of our analyses we will focus on a comparison of the best-resolved voids. These are the largest voids in the images, and here we restrict the analyses to only those voids with radii ≥ 10 pixels (corresponding to a radius $\geq 20h^{-1}$ Mpc). Because large voids are rare, these represent only a small fraction of the total number of voids in the samples (15,063 in the simulated sample and 16,165 in the generated sample). However, unlike the smallest voids (which are poorly resolved), these largest voids are sufficiently well resolved to allow a computation of their radial density profiles.

For comparison with our complete samples of voids shown in Figure 6, Figure 7 shows the same normalized probability distributions, but using only the largest voids. Compared to the results in Figure 6, there is a much greater difference between the distributions of void radii and void effective radii in Figure 7. This is due to a combination of two effects that go into assigning each void its final area (from which the effective radius is determined). First, the larger holes have a larger number of underdense pixels just outside their circumferences than do the smaller holes. Therefore, a large hole that has been identified as being a void has a higher probability of having its final area enhanced relative to the area of the hole (i.e., by the addition of pixels from smaller holes that overlap the large hole by a significant amount). This necessarily increases the effective radius of a void with an enhanced area.

In addition, because of their relatively large size, the probability of the largest voids in a given image overlapping one another by a small amount is higher than the probability of the smallest voids in a given image overlapping by a similar amount. In the case of these small overlaps ($\leq 10\%$ of the area of the smallest of the two associated holes), the overlap area is assigned to the larger
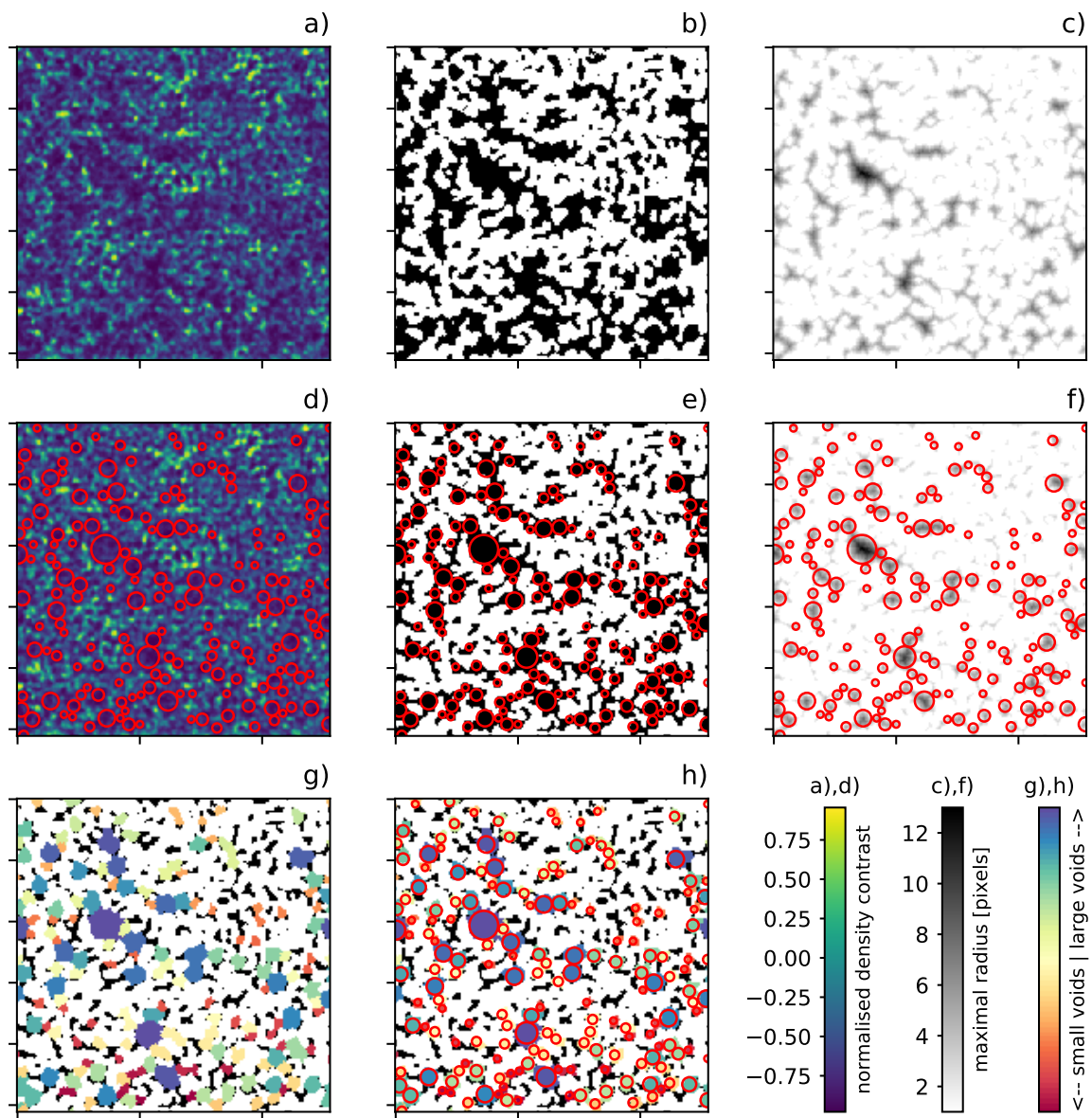
Figure 5: Illustration of the *voidfinder* algorithm: a) normalized mass density, b) locations of wall pixels (white) and void pixels (black), c) maximal radius for each void pixel, d) – f) largest hole contained within each void, overlaid on the panels directly above (red circles), g) final void areas overlaid on the wall/void pixel distribution, h) same as (g), but with the largest hole contained within each void superposed on the image.
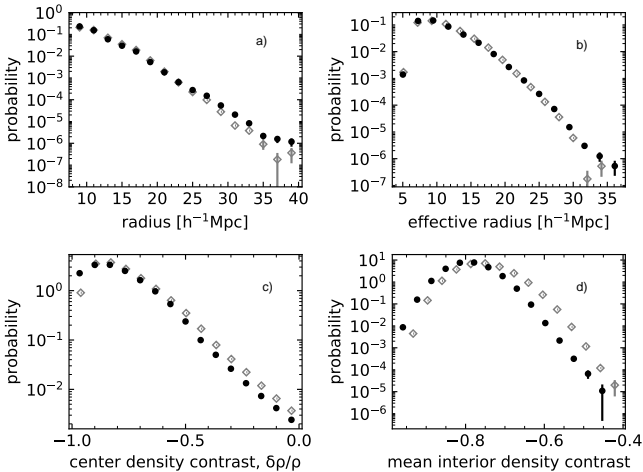
11

Figure 6: Normalized probability distributions for various void properties: a) void radii, b) void effective radii, c) value of the density contrast at the centers of the voids, d) mean interior density contrast, computed using the final areas of the voids. Diamonds: results from images obtained with the WGAN. Circles: results from images obtained from N-body simulations. Error bars are omitted when they are comparable to or smaller than the sizes of the data points.

Figure 7: Same as Figure 6, but here only voids with radius $\geq 20h^{-1}$ Mpc are used.

void, resulting in the smaller of the two voids having a final area that is reduced compared to the size of its hole (and hence, having an effective radius smaller than the radius of its associated hole). From Figure 7a), the median values of the void radii ($20.0h^{-1}$ Mpc) are identical in the simulated and generated images. Similarly, the void effective radii ($21.4h^{-1}$ Mpc) are identical in the simulated and generated images (see Figure 7b).

Figure 7c) shows trends that are similar to those in Figure 6c). While the median central densities of the largest voids are similar in both the simulated and the generated images (-0.82 for the simulated images vs. -0.81 for the generated images), the generated images produce far fewer of the largest voids with central densities ~ -1. Like the complete void sample, the generated images also produce somewhat more large voids with central densities greater than ~ -1, but the range over which this occurs (~ -0.9 to ~ -0.75) is smaller than in the full sample. Figure 7d) also shows trends that are similar to those in Figure 6d). The median values of the distributions in Figure 7d) are similar (-0.80 for the simulated images vs. -0.76 for the generated images), and there is a clear offset between the two distributions such that the mean density contrast of the largest generated voids is systematically higher than that of the largest simulated voids.

Lastly, Figure 8 shows the mean radial underdensity profiles for the largest voids, plotted in terms of dimensionless distance relative to the void radius, (r/r_v). As expected, the central regions of the voids are extremely underdense and the density contrast increases with radius from the void centers. While the radial underdensity profiles are similar in both the simulated and generated images, there are clear differences. For distances $r \lesssim 0.6r_v$,
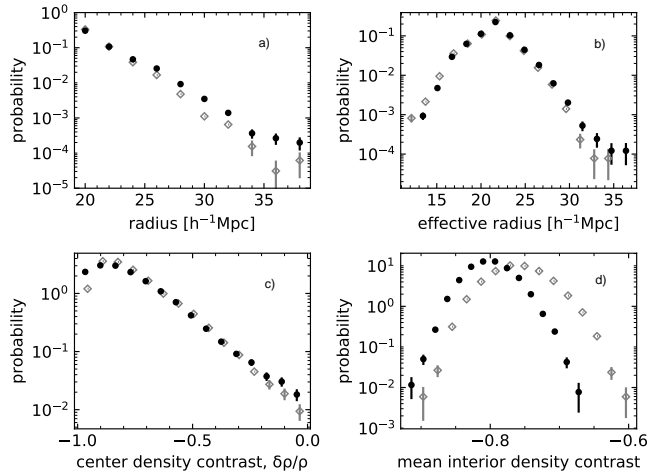
the underdensities of the generated voids are somewhat higher than the underdensities of the simulated voids. For distances $r \gtrsim 0.6r_v$, the sense of the disagreement reverses, with the underdensities of the generated voids being somewhat lower than the underdensities of the simulated voids.

4. Discussion

We used a standard deep convolutional Wasserstein GAN (WGAN) to generate novel 2D images of the smoothed mass density field of a ΛCDM universe, and we explored the use of void statistics as a possible method for assessing and fine-tuning GAN performance. The WGAN was trained using 15,000 2D images of the large-scale structure that were obtained from N-body simulations. The trained WGAN was used to generate 15,000 2D images and a *voidfinder* algorithm, modified to identify regions of low mass density (as opposed to regions of low galaxy density), was then used to create void catalogs from the simulated and generated images. The simulated and generated images yield a similar number of voids (2.5 million voids and 2.8 million voids, respectively).

Within the formal error bars, the mean void properties (i.e., mean radius, mean effective radius, mean central density contrast, and mean interior density contrast) in the simulated and generated images are consistent with each other. Systematic differences between the distributions of the void properties are, however, apparent. Compared to the simulated images, the generated images yield somewhat fewer of the smallest voids and significantly fewer voids with central density contrast ~ -1. Overall, the generated images yield fewer of the emptiest voids and, as a result, the distribution of mean interior density contrast for the generated voids is offset systematically from the distribution of mean interior density contrast for the simulated voids.
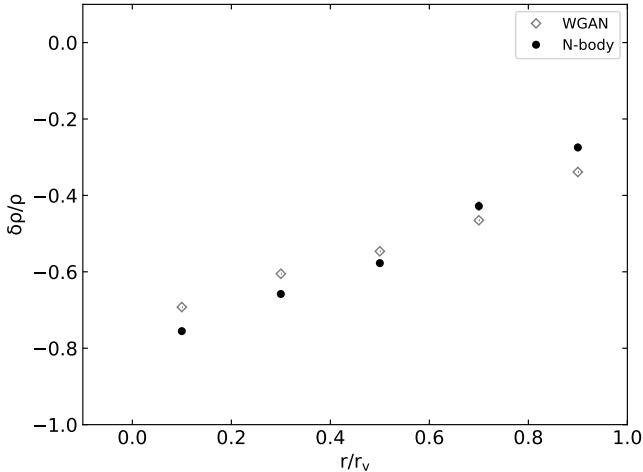
Figure 8: Mean radial underdensity profiles of largest voids, plotted as a function of dimensionless distance relative to the void centers, (r/r_v). Error bars are omitted because they are comparable to or smaller than the data points.

ters used in the generator and critic networks. The use of inception blocks (see Szegedy et al. 2015), for example, would help the network to pick up features of varying sizes by scanning the input layer with kernels of varying sizes. This alone might resolve the issue of the centers of the generated voids being insuffciently underdense. Finally, it will be interesting to see whether more sophisticated network architectures, such as the one used by Kodi Ramanah et al. (2020) to generate large-scale structure maps, yield improved results for the statistics of generated voids.

Acknowledgements

Funding

Neural networks function by learning the average trends in the target distribution but they struggle to capture absolute patterns in the data (see, e.g., Li et al. 2018 for a detailed discussion). That is, our deep convolutional WGAN is clearly able to detect trends in the pixel-to-pixel variations of the smoothed density contrast, but it is not reliably capturing the absolute highs and lows. The effect of this on void properties manifests in Figures 6c) and 7c), where the images yield significantly fewer voids with central density constrast ~ -1 than do the simulated images. The inability of the WGAN to reliably capture the absolute highs and lows of the smoothed density contrast also explains the systematic offsets between the distribution of mean interior density contrast for the generated and simulated images in Figures 6d) and 7d).

GANs present an opportunity to investigate the distribution of the largest structures in Gpc-scale simulations without the need for as many computationally expensive Gpc-scale N-body simulations as would otherwise be necessary. In order for GANs to become a truly viable alternative to simulations, however, they need to be able to fully reproduce the structure that is seen in typical N-body simulations, including the frequency and properties of voids. Because of this, void statistics are a natural higher-order test of the validity of GAN-generated maps of large-scale.

While our WGAN produced voids with properties that were in broad general agreement with the properties of voids in N-body simulations, the systematic differences between the populations are an indication that improvements in the WGAN approach are still necessary. For future work, the network architecture will need to be optimized in such a way that it allows the trained WGAN to better capture absolute trends in the target images. Such optimization may be dependent on the size of the convolutional kernels and/or the values of the hyperparame-

References

Abadi, M., Barham, P., Chen, J., Chen, Z., Davis, A., Dean, J., Devin, M., Ghemawat, S., Irving, G., Isard, M., Kudlur, M., Levenberg, J., Monga, R., Moore, S., Murray, D.G., Steiner, B., Tucker, P., Vasudevan, V., Warden, P., Wicke, M., Yu, Y., Zheng, X., 2016. Tensorflow: A system for large-scale machine learning, in: Keeton, K., Roscoe, T. (Eds.), Proc. of the 12th USENIX Symposium on Operating Systems Design and Implementation, USENIX Association, Berkeley, California, USA. p. 265.

Arjovsky, M., Chintala, S., Bottou, L., 2017. Wasserstein generative adversarial networks, in: Precup, D., Teh, Y.W. (Eds.), Proc. of the 34th International Conference on Machine Learning, Journal of Machine Learning Research, Inc., Brookline, Massachusetts, USA. p. 214.

Aubert, M., Cousinou, M.C., Escoffier, S., Hawken, A.J., Nadathur, S., Alam, S., Bautista, J., Burtin, E., de Mattia, A., Gil-Marín, H., Hou, J., Jullo, E., Neveux, R., Rossi, G., Smith, A., Tamone, A., Vargas Magaña, M., 2020. The Completed SDSS-IV Extended Baryon Oscillation Spectroscopic Survey: Growth rate of structure measurement from cosmic voids. arXiv e-prints , arXiv:2007.09013 2007.09013.

Cai, Y.C., Padilla, N., Li, B., 2015. Testing gravity using cosmic voids. MNRAS 451, 1036–1055. 1410.1510.

Clampitt, J., Cai, Y.C., Li, B., 2013. Voids in modified gravity: excursion set predictions. MNRAS 431, 749–766. 1212.2216.

Curtis, O., Brainerd, T.G., 2020. Fast Generation of Large-scale Structure Density Maps via Generative Adversarial Networks. Research Notes of the American Astronomical Society 4, 90. 2006.11359.

Davis, M., Efstathiou, G., Frenk, C.S., White, S.D.M., 1985. The evolution of large-scale structure in a universe dominated by cold dark matter. ApJ 292, 371–394.

DESI Collaboration, Aghamousa, A., Aguilar, J., Ahlen, S., Alam, S., Allen, L.E., Allende Prieto, C., Annis, J., Bailey, S., Balland, C., Ballester, O., Baltay, C., Beaufore, L., Bebek, C., Beers, T.C., Bell, E.F., Bernal, J.L., Besuner, R., Beutler, F., Blake, C., Bleuler, H., Blomqvist, M., Blum, R., Bolton, A.S., Briceno, C., Brooks, D., Brownstein, J.R., Buckley-Geer, E., Burden, A., Burtin, E., Busca, N.G., Cahn, R.N., Cai, Y.C., Cardiel-Sas, L., Carlberg, R.G., Carton, P.H., Casas, R., Castander, F.J., Cervantes-Cota, J.L., Claybaugh, T.M., Close, M., Coker, C.T., Cole, S., Comparat, J., Cooper, A.P., Cousinou, M.C., Crocce,

M., Cuby, J.G., Cunningham, D.P., Davis, T.M., Dawson, K.S., de la Macorra, A., De Vicente, J., Delubac, T., Derwent, M., Dey, A., Dhungana, G., Ding, Z., Doel, P., Duan, Y.T., Ealet, A., Edelstein, J., Eftekharzadeh, S., Eisenstein, D.J., Elliott, A., Escoffier, S., Evatt, M., Fagrelius, P., Fan, X., Fanning, K., Farahi, A., Farihi, J., Favole, G., Feng, Y., Fernandez, E., Findlay, J.R., Finkbeiner, D.P., Fitzpatrick, M.J., Flaugher, B., Flender, S., Font-Ribera, A., Forero-Romero, J.E., Fosalba, P., Frenk, C.S., Fumagalli, M., Gaensicke, B.T., Gallo, G., Garcia-Bellido, J., Gaztanaga, E., Pietro Gentile Fusillo, N., Gerard, T., Gershkovich, I., Giannantonio, T., Gillet, D., Gonzalez-de-Rivera, G., Gonzalez-Perez, V., Gott, S., Graur, O., Gutierrez, G., Guy, J., Habib, S., Heetderks, H., Heetderks, I., Heitmann, K., Hellwing, W.A., Herrera, D.A., Ho, S., Holland, S., Honscheid, K., Huff, E., Hutchinson, T.A., Huterer, D., Hwang, H.S., Illa Laguna, J.M., Ishikawa, Y., Jacobs, D., Jeffrey, N., Jelinsky, P., Jennings, E., Jiang, L., Jimenez, J., Johnson, J., Joyce, R., Jullo, E., Juneau, S., Kama, S., Karcher, A., Karkar, S., Kehoe, R., Kennamer, N., Kent, S., Kilbinger, M., Kim, A.G., Kirkby, D., Kisner, T., Kitanidis, E., Kneib, J.P., Koposov, S., Kovacs, E., Koyama, K., Kremin, A., Kron, R., Kronig, L., Kueter-Young, A., Lacey, C.G., Lafever, R., Lahav, O., Lambert, A., Lampton, M., Landriau, M., Lang, D., Lauer, T.R., Le Goff, J.M., Le Guillou, L., Le Van Suu, A., Lee, J.H., Lee, S.J., Leitner, D., Lesser, M., Levi, M.E., L'Huillier, B., Li, B., Liang, M., Lin, H., Linder, E., Loebman, S.R., Lukić, Z., Ma, J., MacCrann, N., Magneville, C., Makarem, L., Manera, M., Manser, C.J., Marshall, R., Martini, P., Massey, R., Matheson, T., McCauley, J., McDonald, P., McGreer, I.D., Meisner, A., Metcalfe, N., Miller, T.N., Miquel, R., Moustakas, J., Myers, A., Naik, M., Newman, J.A., Nichol, R.C., Nicola, A., Nicolati da Costa, L., Nie, J., Niz, G., Norberg, P., Nord, B., Norman, D., Nugent, P., O'Brien, T., Oh, M., Olsen, K.A.G., Padilla, C., Padmanabhan, H., Padmanabhan, N., Palanque-Delabrouille, N., Palmese, A., Pappalardo, D., Pâris, I., Park, C., Patej, A., Peacock, J.A., Peiris, H.V., Peng, X., Percival, W.J., Perruchot, S., Pieri, M.M., Pogge, R., Pollack, J.E., Poppett, C., Prada, F., Prakash, A., Probst, R.G., Rabinowitz, D., Raichoor, A., Ree, C.H., Refregier, A., Regal, X., Reid, B., Reil, K., Rezaie, M., Rockosi, C.M., Roe, N., Ronayette, S., Roodman, A., Ross, A.J., Ross, N.P., Rossi, G., Rozo, E., Ruhlmann-Kleider, V., Rykoff, E.S., Sabiu, C., Samushia, L., Sanchez, E., Sanchez, J., Schlegel, D.J., Schneider, M., Schubnell, M., Secroun, A., Seljak, U., Seo, H.J., Serrano, S., Shafieloo, A., Shan, H., Sharples, R., Sholl, M.J., Shourt, W.V., Silber, J.H., Silva, D.R., Sirk, M.M., Slosar, A., Smith, A., Smoot, G.F., Som, D., Song, Y.S., Sprayberry, D., Staten, R., Stefanik, A., Tarle, G., Sien Tie, S., Tinker, J.L., Tojeiro, R., Valdes, F., Valenzuela, O., Valluri, M., Vargas-Magana, M., Verde, L., Walker, A.R., Wang, J., Wang, Y., Weaver, B.A., Weaverdyck, C., Wechsler, R.H., Weinberg, D.H., White, M., Yang, Q., Yeche, C., Zhang, T., Zhao, G.B., Zheng, Y., Zhou, X., Zhou, Z., Zhu, Y., Zou, H., Zu, Y., 2016. The DESI Experiment Part I: Science,Targeting, and Survey Design. arXiv e-prints , arXiv:1611.00036$1611.00036$.

Doré, O., Werner, M.W., Ashby, M.L.N., Bleem, L.E., Bock, J., Burt, J., Capak, P., Chang, T.C., Chaves-Montero, J., Chen, C.H., Civano, F., Cleeves, I.I., Cooray, A., Crill, B., Crossfield, I.J.M., Cushing, M., de la Torre, S., DiMatteo, T., Dvory, N., Dvorkin, C., Espaillat, C., Ferraro, S., Finkbeiner, D., Greene, J., Hewitt, J., Hogg, D.W., Huffenberger, K., Jun, H.S., Ilbert, O., Jeong, W.S., Johnson, J., Kim, M., Kirkpatrick, J.D., Kowalski, T., Korngut, P., Li, J., Lisse, C.M., MacGregor, M., Mamajek, E.E., Mauskopf, P., Melnick, G., Ménard, B., Neyrinck, M., Öberg, K., Pisani, A., Rocca, J., Salvato, M., Schaan, E., Scoville, N.Z., Song, Y.S., Stevens, D.J., Tenneti, A., Teplitz, H., Tolls, V., Unwin, S., Urry, M., Wandelt, B., Williams, B.F., Wilner, D., Windhorst, R.A., Wolk, S., Yorke, H.W., Zemcov, M., 2018. Science Impacts of the SPHEREx All-Sky Optical to Near-Infrared Spectral Survey II: Report of a Community Workshop on the Scientific Synergies Between the SPHEREx Survey and Other Astronomy Observatories. arXiv e-prints , arXiv:1805.05489$1805.05489$.

Douglass, K.A., Vogeley, M.S., 2017. Determining the Large-scale Environmental Dependence of Gas-phase Metallicity in Dwarf Galaxies. ApJ 834, 186. 1604.08599.

El-Ad, H., Piran, T., 1997. Voids in the Large-Scale Structure. ApJ 491, 421–435. astro-ph/9702135.

Falck, B., Koyama, K., Zhao, G.B., Cautun, M., 2018. Using voids to unscreen modified gravity. MNRAS 475, 3262–3272. 1704.08942.

Falck, B., Wang, J., Jenkins, A., Lemson, G., Medvedev, D., Neyrinck, M.C., Szalay, A.S., 2021. Indra: a Public Computationally-Accessible Suite of Cosmological N-body Simulations. arXiv e-prints , arXiv:2101.03631$2101.03631$.

Feder, R.M., Berger, P., Stein, G., 2020. Nonlinear 3D cosmic web simulation with heavy-tailed generative adversarial networks. Phys. Rev. D 102, 103504. 2005.03050.

Gan, F.K., Bekki, K., Hashemizadeh, A., 2021. SeeingGAN: Galactic image deblurring with deep learning for better morphological classification of galaxies. arXiv e-prints , arXiv:2103.09711$2103.09711$.

Giovanelli, R., Haynes, M.P., 1991. Redshift surveys of galaxies. ARAA 29, 499–541.

Glorot, X., Bengio, Y., 2010. Understanding the difficulty of training deep feedforward neural networks, in: Teh, Y.W., Titterington, M. (Eds.), Proc. of the Thirteenth International Conference on Artificial Intelligence and Statistics, Journal of Machine Learning Research Inc., Brookline, Massachusetts, USA. p. 249.

Goldberg, D.M., Vogeley, M.S., 2004. Simulating Voids. ApJ 605, 1–6. astro-ph/0307191.

Goodfellow, I., Pouget-Abadie, J., Mirza, M., Xu, B., Warde-Farley, D., Ozair, S., Courville, A., Bengio, Y., 2020. Generative adversarial networks. Communications of the Association for Computing Machinery 63, 139.

Gulrajani, I., Ahmed, F., Arjovsky, M., Dumoulin, V., Courville, A., 2017. Improved training of wasserstein gans, in: von Luxburg, U., Guyon, I., Bengio, S., Wallach, H., Fergus, R. (Eds.), Proc. of the 31st International Conference on Neural Information Processing Systems, Curran Associates Inc., Red Hook, NY, USA. p. 5769.

Hamaus, N., Cousinou, M.C., Pisani, A., Aubert, M., Escoffier, S., Weller, J., 2017. Multipole analysis of redshift-space distortions around cosmic voids. JCAP 2017, 014. 1705.05328.

Hamaus, N., Sutter, P.M., Wandelt, B.D., 2014. Universal Density Profile for Cosmic Voids. Phys. Rev. Letters 112, 251302. 1403.5499.

Hoyle, F., Rojas, R.R., Vogeley, M.S., Brinkmann, J., 2005. The Luminosity Function of Void Galaxies in the Sloan Digital Sky Survey. ApJ 620, 618–628. astro-ph/0309728.

Hoyle, F., Vogeley, M.S., 2004. Voids in the Two-Degree Field Galaxy Redshift Survey. ApJ 607, 751–764. astro-ph/0312533.

Kim, J., Park, C., Rossi, G., Lee, S.M., Gott, J. Richard, I., 2011. The New Horizon Run Cosmological N-Body Simulations. Journal of Korean Astronomical Society 44, 217–234. 1112.1754.

Kingma, D.P., Ba, J., 2015. Adam: A method for stochastic optimization, in: Bengio, Y., LeCun, Y. (Eds.), Proc. of the 3rd International Conference on Learning Representations, International Conference on Learning Representations, San Diego, California, USA.

Kodi Ramanah, D., Charnock, T., Villaescusa-Navarro, F., Wandelt, B.D., 2020. Super-resolution emulator of cosmological simulations using deep physical models. MNRAS 495, 4227–4236. 2001.05519.

Kreckel, K., Platen, E., Aragón-Calvo, M.A., van Gorkom, J.H., van de Weygaert, R., van der Hulst, J.M., Beygu, B., 2012. The Void Galaxy Survey: Optical Properties and H I Morphology and Kinematics. AJ 144, 16. 1204.5185.

Lachieze-Rey, M., da Costa, L.N., Maurogordato, S., 1992. Void Probability Function in the Southern Sky Redshift Survey. ApJ 399, 10.

Laureijs, R., Amiaux, J., Arduini, S., Auguères, J.L., Brinchmann, J., Cole, R., Cropper, M., Dabin, C., Duvet, L., Ealet, A., Garilli, B., Gondoin, P., Guzzo, L., Hoar, J., Hoekstra, H., Holmes, R., Kitching, T., Maciaszek, T., Mellier, Y., Pasian, F., Percival, W., Rhodes, J., Saavedra Criado, G., Sauvage, M., Scaramella, R., Valenziano, L., Warren, S., Bender, R., Castander, F., Cimatti,

14

A., Le Fèvre, O., Kurki-Suonio, H., Levi, M., Lilje, P., Meylan, G., Nichol, R., Pedersen, K., Popa, V., Rebolo Lopez, R., Rix, H.W., Rottgering, H., Zeilinger, W., Grupp, F., Hudelot, P., Massey, R., Meneghetti, M., Miller, L., Paltani, S., Paulin-Henriksson, S., Pires, S., Saxton, C., Schrabback, T., Seidel, G., Walsh, J., Aghanim, N., Amendola, L., Bartlett, J., Baccigalupi, C., Beaulieu, J.P., Benabed, K., Cuby, J.G., Elbaz, D., Fosalba, P., Gavazzi, G., Helmi, A., Hook, I., Irwin, M., Kneib, J.P., Kunz, M., Mannucci, F., Moscardini, L., Tao, C., Teyssier, R., Weller, J., Zamorani, G., Zapatero Osorio, M.R., Boulade, O., Foumond, J.J., Di Giorgio, A., Guttridge, P., James, A., Kemp, M., Martignac, J., Spencer, A., Walton, D., Blümchen, T., Bonoli, C., Bortoletto, F., Cerna, C., Corcione, L., Fabron, C., Jahnke, K., Ligori, S., Madrid, F., Martin, L., Morgante, G., Pamplona, T., Prieto, E., Riva, M., Toledo, R., Trifoglio, M., Zerbi, F., Abdalla, F., Douspis, M., Grenet, C., Borgani, S., Bouwens, R., Courbin, F., Delouis, J.M., Dubath, P., Fontana, A., Frailis, M., Grazian, A., Koppenhöfer, J., Mansutti, O., Melchior, M., Mignoli, M., Mohr, J., Neissner, C., Noddle, K., Poncet, M., Scodeggio, M., Serrano, S., Shane, N., Starck, J.L., Surace, C., Taylor, A., Verdoes-Kleijn, G., Vuerli, C., Williams, O.R., Zacchei, A., Altieri, B., Escudero Sanz, I., Kohley, R., Oosterbroek, T., Astier, P., Bacon, D., Bardelli, S., Baugh, C., Bellagamba, F., Benoist, C., Bianchi, D., Biviano, A., Branchini, E., Carbone, C., Cardone, V., Clements, D., Colombi, S., Conselice, C., Cresci, G., Deacon, N., Dunlop, J., Fedeli, C., Fontanot, F., Franzetti, P., Giocoli, C., Garcia-Bellido, J., Gow, J., Heavens, A., Hewett, P., Heymans, C., Holland, A., Huang, Z., Ilbert, O., Joachimi, B., Jennins, E., Kerins, E., Kiessling, A., Kirk, D., Kotak, R., Krause, O., Lahav, O., van Leeuwen, F., Lesgourgues, J., Lombardi, M., Magliocchetti, M., Maguire, K., Majerotto, E., Maoli, R., Marulli, F., Maurogordato, S., McCracken, H., McLure, R., Melchiorri, A., Merson, A., Moresco, M., Nonino, M., Norberg, P., Peacock, J., Pello, R., Penny, M., Pettorino, V., Di Porto, C., Pozzetti, L., Quercellini, C., Radovich, M., Rassat, A., Roche, N., Ronayette, S., Rossetti, E., Sartoris, B., Schneider, P., Semboloni, E., Serjeant, S., Simpson, F., Skordis, C., Smadja, G., Smartt, S., Spano, P., Spiro, S., Sullivan, M., Tilquin, A., Trotta, R., Verde, L., Wang, Y., Williger, G., Zhao, G., Zoubian, J., Zucca, E., 2011. Euclid Definition Study Report. arXiv e-prints , arXiv:1110.3193`1110.3193`.

Li, B., Zhao, G.B., Koyama, K., 2012. Haloes and voids in f(R) gravity. MNRAS 421, 3481–3487. `1111.2602`.

Li, Y., Yu, R., Shahabi, C., Liu, Y., 2018. Diffusion convolutional recurrent neural network: Data-driven traffic forecasting, in: Bengio, Y., LeCun, Y. (Eds.), Proc. of the 6th International Conference on Learning Representations, International Conference on Learning Representations, San Diego, California, USA.

Mao, Q., Berlind, A.A., Scherrer, R.J., Neyrinck, M.C., Scoccimarro, R., Tinker, J.L., McBride, C.K., Schneider, D.P., Pan, K., Bizyaev, D., Malanushenko, E., Malanushenko, V., 2017. A Cosmic Void Catalog of SDSS DR12 BOSS Galaxies. ApJ 835, 161. `1602.02771`.

Mustafa, M., Bard, D., Bhimji, W., Lukić, Z., Al-Rfou, R., Kratochvil, J.M., 2019. CosmoGAN: creating high-fidelity weak lensing convergence maps using Generative Adversarial Networks. Computational Astrophysics and Cosmology 6, 1. `1706.02390`.

Oliphant, T.E., 2007. Python for scientific computing. Computing in Science & Engineering 9, 10–20.

Rodríguez, A.C., Kacprzak, T., Lucchi, A., Amara, A., Sgier, R., Fluri, J., Hofmann, T., Réfrégier, A., 2018. Fast cosmic web simulations with generative adversarial networks. Computational Astrophysics and Cosmology 5, 4. `1801.09070`.

Sahlén, M., 2019. Cluster-void degeneracy breaking: Neutrino properties and dark energy. Phys. Rev. D 99, 063525. `1807.02470`.

Sánchez, C., Clampitt, J., Kovacs, A., Jain, B., García-Bellido, J., Nadathur, S., Gruen, D., Hamaus, N., Huterer, D., Vielzeuf, P., Amara, A., Bonnett, C., DeRose, J., Hartley, W.G., Jarvis, M., Lahav, O., Miquel, R., Rozo, E., Rykoff, E.S., Sheldon, E., Wechsler, R.H., Zuntz, J., Abbott, T.M.C., Abdalla, F.B., Annis, J., Benoit-Lévy, A., Bernstein, G.M., Bernstein, R.A., Bertin, E., Brooks, D., Buckley-Geer, E., Carnero Rosell, A., Carrasco

Kind, M., Carretero, J., Crocce, M., Cunha, C.E., D'Andrea, C.B., da Costa, L.N., Desai, S., Diehl, H.T., Dietrich, J.P., Doel, P., Evrard, A.E., Fausti Neto, A., Flaugher, B., Fosalba, P., Frieman, J., Gaztanaga, E., Gruendl, R.A., Gutierrez, G., Honscheid, K., James, D.J., Krause, E., Kuehn, K., Lima, M., Maia, M.A.G., Marshall, J.L., Melchior, P., Plazas, A.A., Reil, K., Romer, A.K., Sanchez, E., Schubnell, M., Sevilla-Noarbe, I., Smith, R.C., Soares-Santos, M., Sobreira, F., Suchyta, E., Tarle, G., Thomas, D., Walker, A.R., Weller, J., DES Collaboration, 2017. Cosmic voids and void lensing in the Dark Energy Survey Science Verification data. MNRAS 465, 746–759. `1605.03982`.

Schawinski, K., Zhang, C., Zhang, H., Fowler, L., Santhanam, G.K., 2017. Generative adversarial networks recover features in astrophysical images of galaxies beyond the deconvolution limit. MNRAS 467, L110–L114. `1702.00403`.

Spergel, D., Gehrels, N., Baltay, C., Bennett, D., Breckinridge, J., Donahue, M., Dressler, A., Gaudi, B.S., Greene, T., Guyon, O., Hirata, C., Kalirai, J., Kasdin, N.J., Macintosh, B., Moos, W., Perlmutter, S., Postman, M., Rauscher, B., Rhodes, J., Wang, Y., Weinberg, D., Benford, D., Hudson, M., Jeong, W.S., Mellier, Y., Traub, W., Yamada, T., Capak, P., Colbert, J., Masters, D., Penny, M., Savransky, D., Stern, D., Zimmerman, N., Barry, R., Bartusek, L., Carpenter, K., Cheng, E., Content, D., Dekens, F., Demers, R., Grady, K., Jackson, C., Kuan, G., Kruk, J., Melton, M., Nemati, B., Parvin, B., Poberezhskiy, I., Peddie, C., Ruffa, J., Wallace, J.K., Whipple, A., Wollack, E., Zhao, F., 2015. Wide-Field InfraRed Survey Telescope-Astrophysics Focused Telescope Assets WFIRST-AFTA 2015 Report. arXiv e-prints , arXiv:1503.03757`1503.03757`.

Springel, V., 2005. The cosmological simulation code GADGET-2. MNRAS 364, 1105–1134. `astro-ph/0505010`.

Springel, V., White, S.D.M., Jenkins, A., Frenk, C.S., Yoshida, N., Gao, L., Navarro, J., Thacker, R., Croton, D., Helly, J., Peacock, J.A., Cole, S., Thomas, P., Couchman, H., Evrard, A., Colberg, J., Pearce, F., 2005. Simulations of the formation, evolution and clustering of galaxies and quasars. Nature 435, 629–636. `astro-ph/0504097`.

Sutter, P.M., Lavaux, G., Wandelt, B.D., Weinberg, D.H., 2012. A Public Void Catalog from the SDSS DR7 Galaxy Redshift Surveys Based on the Watershed Transform. ApJ 761, 44. `1207.2524`.

Szegedy, C., Liu, W., Jia, Y., Sermanet, P., Reed, S., Anguelov, D., Erhan, D., Vanhoucke, V., Rabinovich, A., 2015. Going deeper with convolutions, in: Baldwin, R. (Ed.), Proc. of the 2015 Institute of Electrical and Electronics Engineers' conference on computer vision and pattern recognition, Institute of Electrical and Electronics Engineers, Los Alamitos, California, USA. p. 1.

Tamura, N., Takato, N., Shimono, A., Moritani, Y., Yabe, K., Ishizuka, Y., Ueda, A., Kamata, Y., Aghazarian, H., Arnouts, S., Barban, G., Barkhouser, R.H., Borges, R.C., Braun, D.F., Carr, M.A., Chabaud, P.Y., Chang, Y.C., Chen, H.Y., Chiba, M., Chou, R.C.Y., Chu, Y.H., Cohen, J., de Almeida, R.P., de Oliveira, A.C., de Oliveira, L.S., Dekany, R.G., Dohlen, K., dos Santos, J.B., dos Santos, L.H., Ellis, R., Fabricius, M., Ferrand, D., Ferreira, D., Golebiowski, M., Greene, J.E., Gross, J., Gunn, J.E., Hammond, R., Harding, A., Hart, M., Heckman, T.M., Hirata, C.M., Ho, P., Hope, S.C., Hovland, L., Hsu, S.F., Hu, Y.S., Huang, P.J., Jaquet, M., Jing, Y., Karr, J., Kimura, M., King, M.E., Komatsu, E., Le Brun, V., Le Fèvre, O., Le Fur, A., Le Mignant, D., Ling, H.H., Loomis, C.P., Lupton, R.H., Madec, F., Mao, P., Marrara, L.S., Mendes de Oliveira, C., Minowa, Y., Morantz, C., Murayama, H., Murray, G.J., Ohyama, Y., Orndorff, J., Pascal, S., Pereira, J.M., Reiley, D., Reinecke, M., Ritter, A., Roberts, M., Schwochert, M.A., Seiffert, M.D., Smee, S.A., Sodre, L., Spergel, D.N., Steinkraus, A.J., Strauss, M.A., Surace, C., Suto, Y., Suzuki, N., Swinbank, J., Tait, P.J., Takada, M., Tamura, T., Tanaka, Y., Tresse, L., Verducci, D., Vibert, D., Vidal, C., Wang, S.Y., Wen, C.Y., Yan, C.H., Yasuda, N., 2016. Prime Focus Spectrograph (PFS) for the Subaru telescope: overview, recent progress, and future perspectives, in: Evans, C.J., Simard, L., Takami, H. (Eds.), Ground-based and Airborne Instrumentation for Astronomy VI, p. 99081M. `1608.01075`.

Tavasoli, S., 2021. Void Galaxy Distribution: A Challenge for ΛCDM. ApJ 916, L24. `2109.10369`.

The LSST Dark Energy Science Collaboration, Mandelbaum, R., Eifler, T., Hložek, R., Collett, T., Gawiser, E., Scolnic, D., Alonso, D., Awan, H., Biswas, R., Blazek, J., Burchat, P., Chisari, N.E., Dell'Antonio, I., Digel, S., Frieman, J., Goldstein, D.A., Hook, I., Ivezić, Ž., Kahn, S.M., Kamath, S., Kirkby, D., Kitching, T., Krause, E., Leget, P.F., Marshall, P.J., Meyers, J., Miyatake, H., Newman, J.A., Nichol, R., Rykoff, E., Sanchez, F.J., Slosar, A., Sullivan, M., Troxel, M.A., 2018. The LSST Dark Energy Science Collaboration (DESC) Science Requirements Document. arXiv e-prints , arXiv:1809.016691809.01669.

Tinker, J.L., Weinberg, D.H., Warren, M.S., 2006. Cosmic Voids and Galaxy Bias in the Halo Occupation Framework. ApJ 647, 737–752. `astro-ph/0603146`.

Vogeley, M.S., Geller, M.J., Park, C., Huchra, J.P., 1994. Voids and Constraints on Nonlinear Clustering of Galaxies. AJ 108, 745.

Walt, S.v.d., Colbert, S.C., Varoquaux, G., 2011. The numpy array: a structure for efficient numerical computation. Computing in Science & Engineering 13, 22–30.

White, S.D.M., 1979. Further simulations of merging galaxies. MNRAS 189, 831–852.

Zingales, T., Waldmann, I.P., 2018. ExoGAN: Retrieving Exoplanetary Atmospheres Using Deep Convolutional Generative Adversarial Networks. AJ 156, 268. `1806.02906`.

Appendix A. Wasserstein GAN

Arjovsky et al. (2017) suggest switching the standard GAN loss function to the Wasserstein metric (a.k.a. the Kantorovich–Rubinstein metric or Earth mover's distance). An intuitive explanation of the Earth mover's distance is found in its name. Imagine trying to relocate a pile of dirt from one location to another. The Earth mover's distance is then the metric that provides the most cost effective way to transport the dirt. For WGANs, the loss function becomes:

$$W(\mathbb{P}_{data}, \mathbb{P}_{gen}) := \inf_{\gamma(x,y)\in\Pi(\mathbb{P}_{data},\mathbb{P}_{gen})} \mathbb{E}_{(x,y)\sim\gamma}[||x-y||] \quad . \tag{A.1}$$

Here, $\Pi(\mathbb{P}_{data}, \mathbb{P}_{gen})$ is the set of all couplings of $\mathbb{P}_{data}$ and $\mathbb{P}_{gen}$. If each distribution is thought to be a unit amount of soil piled over a metric space, then $\gamma(x,y)$ represents how much soil must be moved from x to y such that $\mathbb{P}_{data}$ becomes $\mathbb{P}_{gen}$. In other words, Equation A.1 reveals the cost of the optimal way to transfer soil.

In practice, solving Equation A.1 is intractable. However, Arjovsky et al. (2017) have shown that the Wasserstein metric reduces to

$$W(\mathbb{P}_{data}, \mathbb{P}_{gen}) := -\mathbb{E}_{\vec{z}\sim p_{prior}(\vec{z})}[f(G_{\theta_G}(\vec{z}))] \quad , \tag{A.2}$$

provided that f exists and is K-Lipschitz. In the WGAN algorithm, f is analogous to the set of weights, w, that parameterize the critic network. In other words, given weights, w, lying in a compact space, W, one back propagates through $\mathbb{E}_{\vec{z}\sim p_{prior}(\vec{z})}[f_w(G_{\theta_G}(\vec{z}))]$ to update the generator's weights, just as one would do in the standard GAN architecture. However, to ensure the weights lie in W, the weights are clipped to a box $W = [-c, c]$, where c is a clipping parameter.

The training algorithm for a WGAN is similar to that of the standard GAN algorithm. Aside from the different loss functions and weight clipping, the only change in the WGAN algorithm is that the critic network has its weights updated an integer times more than the does the generator network (i.e., in the standard GAN architecture, both G and D are updated evenly). This change is possible because, unlike the Jensen-Shannon Divergence, the Earth mover's distance is continuous and differentiable everywhere.

Allowing the critic to train in a more stable manner makes mode collapse improbable in the WGAN architecture. This is due to the fact that the critic is no longer trained on how well it can discriminate between real and fake images. Rather, the critic is trained on how it scores the realness or fakeness of an image. Training the critic in this way improves network stability by giving the generator better feedback on how to update its weights.